



CHORUS

This is the accepted manuscript made available via CHORUS. The article has been published as:

Pressure-driven Lifshitz transition in type-II Dirac semimetal NiTe_2

Mengyao Qi, Chao An, Yonghui Zhou, Hao Wu, Bowen Zhang, Chunhua Chen, Yifang Yuan, Shuyang Wang, Ying Zhou, Xuliang Chen, Ranran Zhang, and Zhaorong Yang

Phys. Rev. B **101**, 115124 — Published 16 March 2020

DOI: [10.1103/PhysRevB.101.115124](https://doi.org/10.1103/PhysRevB.101.115124)

1 **Pressure-driven Lifshitz transition in type-II Dirac semimetal NiTe₂**

2
3 Mengyao Qi^{1,2}, Chao An¹, Yonghui Zhou^{2†}, Hao Wu², Bowen Zhang^{2,3}, Chunhua
4 Chen^{2,3}, Yifang Yuan^{2,3}, Shuyang Wang^{2,3}, Ying Zhou¹, Xuliang Chen², Ranran Zhang²,
5 and Zhaorong Yang^{1,2,4†}

6
7 ¹ Institutes of Physical Science and Information Technology, Anhui University,
8 Hefei 230601, China

9 ² Anhui Province Key Laboratory of Condensed Matter Physics at Extreme
10 Conditions, High Magnetic Field Laboratory, Chinese Academy of Sciences, Hefei
11 230031, China

12 ³ Science Island Branch of Graduate School, University of Science and
13 Technology of China, Hefei 230026, China

14 ⁴ Collaborative Innovation Center of Advanced Microstructures, Nanjing
15 University, Nanjing 210093, China

16
17
18
19
20
21
22
23
24
25
26
27
28 †Corresponding author. Email: yhzhou@hmfl.ac.cn; zryang@issp.ac.cn

30 **Abstract**

31 Band engineering in layered transition metal dichalcogenides (TMDs) leads to a
32 variety of emergent phenomena and has obtained considerable attention recently.
33 Transition metal ditelluride NiTe_2 has been discovered experimentally to be a type-II
34 Dirac semimetal at ambient pressure, and was predicted to display superconductivity
35 in the monolayer limit. Here we systematically investigate the structural and
36 electronic properties of type-II Dirac semimetal NiTe_2 under high pressure.
37 Room-temperature synchrotron x-ray diffraction and Raman scattering measurements
38 reveal the stability of pristine hexagonal phase up to 52.2 GPa, whereas both pressure
39 coefficient and linewidth of Raman mode E_g exhibit anomalies at a critical pressure P_c
40 ~ 16 GPa. Meantime, Hall resistivity measurement indicates that the hole-dominated
41 behavior maintains up to 15.6 GPa and transforms into electron-dominated at higher
42 pressures. Our findings consistently demonstrate a pressure-induced Lifshitz
43 transition in type-II Dirac semimetal NiTe_2 .

44

45 Layered transition metal dichalcogenides (TMDs) have attracted extensive interest
46 because of their rich physical properties [1-3] and potential applications in electronics
47 and optoelectronics [4]. TMDs have a general formula MX_2 (M = transition metal, X
48 = S, Se or Te), where the adjacent X-M-X layers are held together by van der Waals
49 interactions [5]. During the past several years, accompanied by exploration of novel
50 topological electronic states, much attention has been paid to the TMDs focusing on
51 their non-trivial band topology, leading to the theoretical prediction and experimental
52 discovery of type-II Weyl semimetal in WTe_2 [6] and MoTe_2 [7], as well as type-II
53 Dirac semimetal in PtSe_2 [8], PdTe_2 [9], and PtTe_2 [10]. Theoretically, the type-II
54 Dirac (Weyl) semimetals possess highly tilted Dirac (Weyl) cones along certain
55 momentum directions due to the violation of Lorentz invariance [6]. The linear energy
56 dispersions of Dirac (Weyl) cones normally result in an ultra-high carrier mobility and
57 large nonsaturating magnetoresistance [11,12], rendering promising applications in
58 electronics and spintronics. Very recently, NiTe_2 has been reported to be a type-II
59 Dirac semimetal through quantum oscillation measurements and band structure
60 calculations [13]. The topological feature in NiTe_2 has been further observed via spin-
61 and angle-resolved photoemission spectroscopy [14]. It is found that the Dirac points
62 of NiTe_2 are located just at ~ 0.02 eV above the Fermi level, more closely than its
63 homologue PdTe_2 (0.5 eV) [15], PtTe_2 (0.8 eV) [10], and PtSe_2 (1.2 eV) [16], which
64 may provide an advantageous platform to study the topological properties of the
65 type-II Dirac semimetals [13,14]. More interesting, based on *ab initio* calculations, it
66 was predicted that monolayer NiTe_2 is an intrinsic superconductor with a $T_c \sim 5.7$ K,
67 while bilayer NiTe_2 intercalated with lithium displays a two-gap superconductivity
68 with a critical temperature $T_c \sim 11.3$ K [17].

69 As one of the fundamental state parameters, pressure has been proved to be an
70 effective and clean way to tune the electronic states of TMDs according to the
71 discoveries such as pressure-induced superconductivity, pressure induced electronic
72 topological transition (ETT) or Lifshitz transition, etc [18-21]. In this work, we
73 performed high-pressure x-ray diffraction (XRD), Raman scattering, and electrical
74 transport measurements on type-II Dirac semimetal NiTe_2 . With increasing pressure

75 up to 71.2 GPa, although no traces of superconductivity have been detected down to
76 1.8 K, we demonstrate a Lifshitz transition instead. The Lifshitz transition, occurring
77 around $P_c \sim 16$ GPa, is not only reflected in the anomalies of pressure coefficient and
78 linewidth of Raman mode E_g , but also revealed by the sign change of Hall coefficient.

79 Experimental details are presented in Supplemental Material [22]. The synthesized
80 NiTe_2 single crystals are characterized by the XRD and EDXS experiments at ambient
81 pressure. As illustrated in Supplemental Fig. S1a, bulk NiTe_2 crystallizes in the
82 layered CdI_2 -type structure with space group $P-3m1$ (No. 164). Figure S1b shows the
83 XRD patterns of NiTe_2 single crystal. The observation of only $(00l)$ diffraction peaks
84 indicates a c -axis orientation of the as-grown crystals. Figure S1c displays the EDXS
85 characterization, from which the real composition is determined to be $\text{NiTe}_{1.98}$.
86 Powder XRD patterns confirm the pure hexagonal phase (see Fig. S1d). The lattice
87 parameters extracted via Le Bail fitting are $a = 3.8776 \text{ \AA}$, $c = 5.2653 \text{ \AA}$, in agreement
88 with the previous report [13]. These results demonstrate the high quality of the sample
89 used here.

90 To check the structural stability of pristine NiTe_2 under pressure, we performed
91 high-pressure powder XRD measurements at room temperature. As shown in Fig. 1a,
92 all the XRD peaks continuously shift towards higher angles without appearing new
93 peaks when the pressure increases up to 52.2 GPa, indicating the absence of structural
94 phase transition in the pressurized NiTe_2 . The XRD patterns under compression can
95 be well indexed with the hexagonal $P-3m1$ phase in Le Bail refinements. A
96 representative refinement of the XRD patterns at 0.5 GPa is presented at the bottom of
97 Fig. 1a. The fitting results of weighted profile factor R_{WP} , profile factor R_p , and
98 goodness-of-fit χ^2 are 2.61%, 1.37%, and 0.08, respectively. The extracted lattice
99 parameters a , c , and axis ratio c/a decrease monotonically with increasing pressure, as
100 shown in Fig. 1b. Upon compression from 0.5 to 52.2 GPa, the parameter a and c
101 decrease by 7.2% and 13.9%, respectively, revealing a large anisotropy of axial
102 compressibility due to the quasi-two-dimensional nature of the lattice. Meanwhile, the
103 overall volume decreases by 25.9%. Figure 1c shows the pressure (P) dependence of
104 volume (V), which can be fitted by the third-order Birch-Murnaghan equation of state

105 [26]: $P = \frac{3}{2}B_0[(V_0/V)^{\frac{7}{3}} - (V_0/V)^{\frac{5}{3}}] \times \left\{1 + \frac{3}{4}(B'_0 - 4) \left[(V_0/V)^{\frac{2}{3}} - 1\right]\right\}$, where V_0 , B_0 ,
106 and B'_0 are the volume, bulk modulus $-V/(dV/dP)$, and first order derivative of the
107 bulk modulus at zero pressure, respectively. The fitting yields $V_0 = 67.9 \pm 0.5 \text{ \AA}^3$, $B_0 =$
108 $53.3 \pm 7.4 \text{ GPa}$, and $B'_0 = 8.1 \pm 0.9$.

109 Raman spectroscopy is an effective and powerful tool in detecting lattice
110 vibrations, which can provide information including electron-phonon coupling, weak
111 lattice distortion and/or structural transition. Bulk NiTe₂ displays a similar 1T
112 structure of TiTe₂ and nine vibrational modes due to the same irreducible
113 representation at the gamma point of Brillouin zone [27]. Figure 2a shows the
114 selective room-temperature Raman spectra of NiTe₂ single crystal at various pressures.
115 At 0.6 GPa, one vibrational mode that can be assigned to E_g mode is detected at ~84
116 cm⁻¹ [13]. As illustrated in the inset of Fig. 2b, the E_g mode involves in-plane atomic
117 vibrations, with the top and bottom Te atoms moving in opposite directions [28]. In
118 line with the stability of the pristine hexagonal phase as revealed by the XRD
119 measurements, the E_g mode shifts gradually to higher frequencies without appearing
120 new peaks with increasing pressure up to 35.7 GPa. Figure 2b and 2c display the
121 pressure-dependent frequency and full width at half maximum (FWHM) obtained
122 from Lorentz fittings of E_g mode. With increasing pressure, one can see that the
123 Raman frequency increases linearly but with different slopes below and above a
124 critical pressure $P_c \sim 16 \text{ GPa}$, as indicated by an arrow in Fig. 2b. Similar to the Refs.
125 [29, 30], the Grüneisen parameter, $\gamma_i = (B_0/\omega_i) \times (d\omega_i/dP)$ with ω_i the i th phonon mode
126 frequency and B_0 the bulk modulus at zero pressure is calculated for the E_g mode.
127 Both the pressure coefficients and Grüneisen parameters before and after P_c are
128 shown in Table S1. Along with the change of pressure coefficient ($d\omega/dP$) from 2.07
129 cm⁻¹ GPa⁻¹ to 0.99 cm⁻¹ GPa⁻¹, the pressure-dependent FWHM exhibits a rather
130 pronounced anomaly around P_c (see Fig. 2c). As we known, the Raman linewidth is
131 inversely proportional to the lifetime of the phonon mode, which involves information
132 of not only phonon-phonon interactions but also the excitation-phonon interactions
133 such as electron-phonon and spin-phonon coupling [31]. As the pressure increases, the

134 linewidth of phonon modes will generally increase. However, for the pressurized
135 NiTe₂, the FWHM of E_g mode exhibits abrupt drop at pressures of 14.8-18.0 GPa.
136 Without occurring a structural transition, the existence of anomalies in the phonon
137 spectrum is reminiscent of pressure-induced ETT or Lifshitz transition, which has
138 been observed in some other transition metal chalcogenides, such as Bi₂Se₃ [32],
139 Bi₂Te₃ [33], Sb₂Te₃ [34], Sb₂Se₃ [35], and TiTe₂ [27].

140 An ETT or Lifshitz transition occurs when an extreme of the electronic band
141 structure crosses the Fermi energy level, which is associated to a Van Hove singularity
142 in the density of states [36]. Therefore, we further conducted high-pressure electrical
143 resistivity measurements to explore for the possible evidence of the Lifshitz transition.
144 Figure 3a shows the temperature-dependent resistivity $\rho(T)$ at various pressures. At
145 0.7 GPa, a metallic behavior is clearly presented in the temperature region from 1.8 to
146 300 K, similar to that at ambient condition [13]. The metallic behavior maintains with
147 increasing pressure up to 71.2 GPa and no traces of superconductivity are detected
148 down to 1.8 K. Note that the recent high-pressure experiments in polycrystalline
149 NiTe₂ discover a superconducting transition without zero resistance between 12.0 and
150 54.5 GPa [37]. We also note that the possible impurities and defects are
151 superconducting under pressure, such as element Te [38]. Meantime, the $\rho(T)$ curve is
152 monotonically shifted upward except in the low-pressure region. The resistivity and
153 magnetoresistance $MR = [(\rho(H) - \rho(0))/\rho(0)] \times 100\%$ at 10 K under various pressure
154 are displayed in Fig. 3b and 3c, respectively. Note that the resistivity of 300 K in Fig.
155 3b shows a minimum around 5 GPa. Since no structural phase transition occurs under
156 high pressure and the structural parameter c/a concomitantly displays a slope change
157 around 5 GPa (see Fig. 1), the anomaly around 5 GPa might be attributed to an ETT.
158 The MR is almost completely suppressed at pressures above 15.6 GPa, but beyond
159 that, no more anomalies associated with the Lifshitz transition can be discerned from
160 Fig. 3.

161 High-pressure Hall resistivity measurements were further carried out to extract the
162 evolution of charge carriers in the pressurized NiTe₂. Figure 4a and 4b show the
163 selective Hall resistivity curves $\rho_{xy}(H)$ measured at 10 K under various pressure,

164 where the magnetic field H is applied perpendicular to the ab -plane. At 0.7 GPa, the
165 $\rho_{xy}(H)$ curve exhibits a nonlinear feature with positive slope, indicating a
166 hole-dominated multiband feature of the electrical transport in agreement with that at
167 ambient pressure [39]. The Hall coefficient R_H , extracted from the slope of $\rho_{xy}(H)$
168 around zero field, decreases monotonically with increasing pressure and changes from
169 positive to negative above 15.6 GPa (see Fig. 4c). The sign change of the R_H
170 demonstrates that the hole-dominated behavior maintains up to 15.6 GPa and
171 transforms into electron-dominated behavior at higher pressures, which further
172 evidences the change of Fermi surface and could be viewed as a signature of the
173 Lifshitz transition. We note that temperature-induced Lifshitz transition in $ZrTe_5$ also
174 involves the change of charge carrier type [40], which is very similar to our case.

175 In summary, we have systematically investigated the pressure effect on the
176 structural and electronic properties of type-II Dirac semimetal $NiTe_2$ by combining
177 synchrotron x-ray diffraction, Raman scattering, and electrical transport
178 measurements. Although the x-ray diffraction results show the stability of pristine
179 hexagonal structure up to 52.2 GPa, both pressure coefficient and linewidth of Raman
180 mode E_g display abnormal behaviors across $P_c \sim 16$ GPa. Our findings unveil a
181 pressure-induced Lifshitz transition of $NiTe_2$ at P_c , which is further supported by the
182 change of charge carrier type through the electrical transport analysis.

183

184 The authors are grateful for the financial support from the National Key Research
185 and Development Program of China (Grant Nos. 2018YFA0305704 and
186 2016YFA0401804), the National Natural Science Foundation of China (Grant Nos.
187 U1632275, 11874362, U1932152, 11704387, 11804341, U1832209, 11804344, and
188 11605276), the Natural Science Foundation of Anhui Province (Grant Nos.
189 1808085MA06 and 1908085QA18), the Users with Excellence Project of Hefei
190 Center CAS (Grant No. 2018HSC-UE012), and the Major Program of Development
191 Foundation of Hefei Center for Physical Science and Technology (Grant No.
192 2018ZYFX002). Y. H. Zhou was supported by the Youth Innovation Promotion
193 Association CAS (Grant No. 2020443). A portion of this work was supported by the
194 High Magnetic Field Laboratory of Anhui Province. The x-ray experiments were
195 performed at HPCAT (Sector 16, BM-D), Advanced Photon Source, Argonne
196 National Laboratory. HPCAT operations are supported by DOE-NNSA under Award
197 No. DE-NA0001974 and DOE-BES under Award No. DE-FG02-99ER45775, with
198 partial instrumentation funding by NSF. The Advanced Photo Source is a U.S.
199 Department of Energy (DOE) Office of Science by Argonne National Laboratory
200 under Contract No. DE-AC02-06CH11357.
201

- 202 [1] A.H. Castro Neto, Phys. Rev. Lett. 86, 4382 (2001).
- 203 [2] X. Qian, J. Liu, L. Fu, Science 346, 1344 (2014).
- 204 [3] Y. Qi, P.G. Naumov, M.N. Ali, C.R. Rajamathi, W. Schnelle, O. Barkalov, M.
205 Hanfland, S.C. Wu, C. Shekhar, Y. Sun, V. Suss, M. Schmidt, U. Schwarz, E. Pippel, P.
206 Werner, R. Hillebrand, T. Forster, E. Kampert, S. Parkin, R.J. Cava, C. Felser, B. Yan,
207 S.A. Medvedev, Nat. Commun. 7, 11038 (2016).
- 208 [4] B.S. de Lima, R.R. de Cassia, F.B. Santos, L.E. Correa, T.W. Grant, A.L.R.
209 Manesco, G.W. Martins, L.T.F. Eleno, M.S. Torikachvili, A.J.S. Machado, Solid State
210 Commun. 283, 27 (2018).
- 211 [5] Q.H. Wang, K. Kalantar-Zadeh, A. Kis, J.N. Coleman, M.S. Strano, Nat. Nanotech.
212 7, 699 (2012).
- 213 [6] Y. Wu, D. Mou, N.H. Jo, K. Sun, L. Huang, S.L. Bud'ko, P.C. Canfield, A.
214 Kaminski, Phys. Rev. B 94, 121113 (2016).
- 215 [7] K. Deng, G. Wan, P. Deng, K. Zhang, S. Ding, E. Wang, M. Yan, H. Huang, H.
216 Zhang, Z. Xu, J. Denlinger, A. Fedorov, H. Yang, W. Duan, H. Yao, Y. Wu, S. Fan, H.
217 Zhang, X. Chen, S. Zhou, Nat. Phys. 12, 1105 (2016).
- 218 [8] K. Zhang, M. Yan, H. Zhang, H. Huang, M. Arita, Z. Sun, W. Duan, Y. Wu, S.
219 Zhou, Phys. Rev. B 96, 125102 (2017).
- 220 [9] A. Sirohi, S. Das, P. Adhikary, R.R. Chowdhury, A. Vashist, Y. Singh, S. Gayen, T.
221 Das, G. Sheet, J. Phys.: Condens. Matter 31, 085701 (2019).
- 222 [10] M. Yan, H. Huang, K. Zhang, E. Wang, W. Yao, K. Deng, G. Wan, H. Zhang, M.
223 Arita, H. Yang, Z. Sun, H. Yao, Y. Wu, S. Fan, W. Duan, S. Zhou, Nat. Commun. 8,
224 257 (2017).
- 225 [11] W. Zheng, R. Schönemann, N. Aryal, Q. Zhou, D. Rhodes, Y.C. Chiu, K.W. Chen,
226 E. Kampert, T. Förster, T.J. Martin, G.T. McCandless, J.Y. Chan, E. Manousakis, L.
227 Balicas, Phys. Rev. B 97, 235154 (2018).
- 228 [12] Z. Huang, W. Zhang, W. Zhang, Mater. 9, 1 (2016).
- 229 [13] C. Xu, B. Li, W. Jiao, W. Zhou, B. Qian, R. Sankar, N.D. Zhigadlo, Y. Qi, D.
230 Qian, F.-C. Chou, X. Xu, Chem. Mater. 30, 4823 (2018).
- 231 [14] B. Ghosh, D. Mondal, C.-N. Kuo, C.S. Lue, J. Nayak, J. Fujii, I. Vobornik, A.
232 Politano, A. Agarwal, Phys. Rev. B 100, 195134 (2019).
- 233 [15] H.J. Noh, J. Jeong, E.J. Cho, K. Kim, B.I. Min, B.G. Park, Phys. Rev. Lett. 119,
234 016401 (2017).

- 235 [16] H. Huang, S. Zhou, W. Duan, *Phys. Rev. B* 94, 121117 (2016).
- 236 [17] F. Zheng, X.-B. Li, Y. Lin, L. Xiong, X. Chen, J. Feng, arXiv:1911.04668 (2019).
- 237 [18] Z. Chi, X. Chen, F. Yen, F. Peng, Y. Zhou, J. Zhu, Y. Zhang, X. Liu, C. Lin, S.
238 Chu, Y. Li, J. Zhao, T. Kagayama, Y. Ma, Z. Yang, *Phys. Rev. Lett.* 120, 037002
239 (2018).
- 240 [19] X.C. Pan, X. Chen, H. Liu, Y. Feng, Z. Wei, Y. Zhou, Z. Chi, L. Pi, F. Yen, F.
241 Song, X. Wan, Z. Yang, B. Wang, G. Wang, Y. Zhang, *Nat. Commun.* 6, 7805 (2015).
- 242 [20] D. Kang, Y. Zhou, W. Yi, C. Yang, J. Guo, Y. Shi, S. Zhang, Z. Wang, C. Zhang,
243 S. Jiang, A. Li, K. Yang, Q. Wu, G. Zhang, L. Sun, Z. Zhao, *Nat. Commun.* 6, 7804
244 (2015).
- 245 [21] F. Liu, J. Li, K. Zhang, S. Peng, H. Huang, M. Yan, N. Li, Q. Zhang, S. Guo, X.
246 Lü, P. Cai, L. Yin, S. Zhou, W. Duan, J. Shen, W. Yang, *Sci. China-Phys. Mech.*
247 *Astron.* 62, 048211 (2018).
- 248 [22] See Supplemental Material at
249 <http://link.aps.org/supplemental/10.1103/PhysRevB.xx> for the experimental details
250 and the supporting data, which includes Refs. [23–25].
- 251 [23] C. Prescher, V.B. Prakapenka, *High Press. Res.* 35, 223 (2015).
- 252 [24] B.A. Hunter, International Union of Crystallography Commission on Powder
253 Diffraction Newsletter 20, (1998).
- 254 [25] H.K. Mao, J. Xu, P.M. Bell, *J. Geophys. Res.* 91, 4673 (1986).
- 255 [26] F. Birch, *Phys. Rev.* 71, 809 (1947).
- 256 [27] V. Rajaji, U. Dutta, P.C. Sreeparvathy, S.C. Sarma, Y.A. Sorb, B. Joseph, S.
257 Sahoo, S.C. Peter, V. Kanchana, C. Narayana, *Phys. Rev. B* 97, 085107 (2018).
- 258 [28] M. O'Brien, N. McEvoy, C. Motta, J.-Y. Zheng, N.C. Berner, J. Kotakoski, K.
259 Elibol, T.J. Pennycook, J.C. Meyer, C. Yim, M. Abid, T. Hallam, J.F. Donegan, S.
260 Sanvito, G.S. Duesberg, *Mater.* 3, 021004 (2016).
- 261 [29] Y.A. Sorb, V. Rajaji, P.S. Malavi, U. Subbarao, P. Halappa, S.C. Peter, S.
262 Karmakar, C. Narayana, *J. Phys.: Condens. Matter* 28, 015602 (2016).
- 263 [30] Y.A. Sorb, N. Subramanian, T.R. Ravindran, *J. Phys.: Condens. Matter* 25,
264 155401 (2013).
- 265 [31] M. Cardona, *High Press. Res.* 24, 17 (2004).
- 266 [32] R. Vilaplana, D. Santamaría-Pérez, O. Gomis, F.J. Manjón, J. González, A.

267 Segura, A. Muñoz, P. Rodríguez-Hernández, E. Pérez-González, V. Marín-Borrás, V.
268 Muñoz-Sanjose, C. Drasar, V. Kucek, Phys. Rev. B 84, 184110 (2011).

269 [33] R. Vilaplana, O. Gomis, F.J. Manjón, A. Segura, E. Pérez-González, P.
270 Rodríguez-Hernández, A. Muñoz, J. González, V. Marín-Borrás, V. Muñoz-Sanjose, C.
271 Drasar, V. Kucek, Phys. Rev. B 84, 104112 (2011).

272 [34] O. Gomis, R. Vilaplana, F.J. Manjón, P. Rodríguez-Hernández, E.
273 Pérez-González, A. Muñoz, V. Kucek, C. Drasar, Phys. Rev. B 84, 174305 (2011).

274 [35] A. Bera, K. Pal, D.V. Muthu, S. Sen, P. Guptasarma, U.V. Waghmare, A.K. Sood,
275 Phys. Rev. Lett. 110, 107401 (2013).

276 [36] I.M. Lifshitz, Sov. Phys. JETP 11, 1130 (1960).

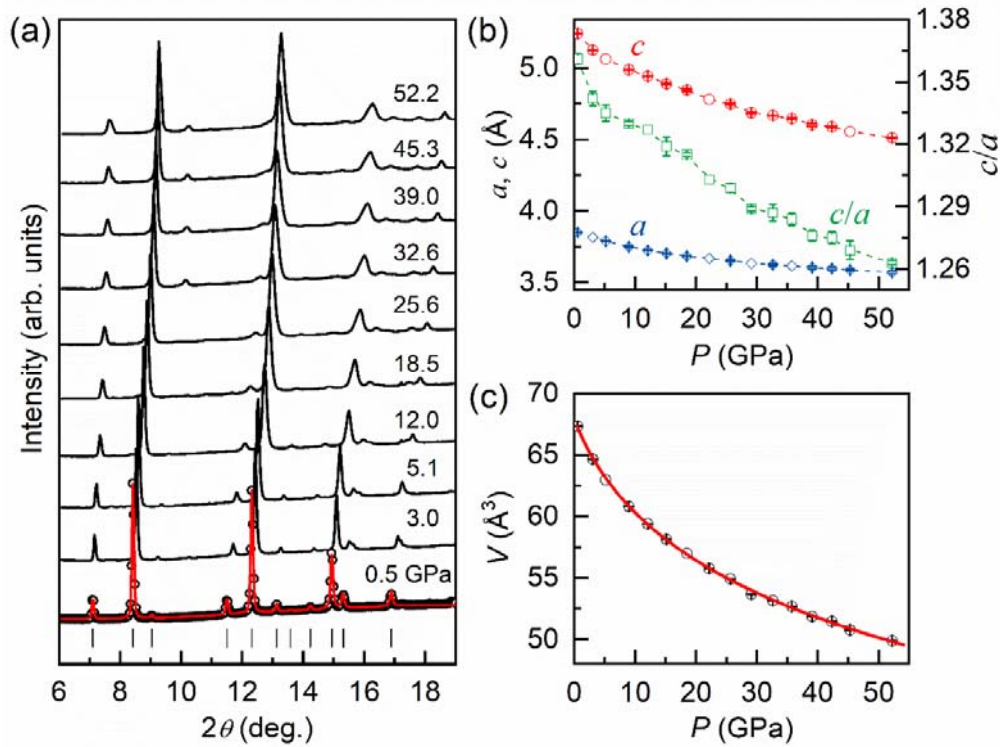
277 [37] T. Li, K. Wang, C. Xu, Q. Hou, H. Wu, J. Ge, S. Cao, J. Zhang, W. Ren, X. Xu, N.
278 Yeh, B. Chen, Z. Feng, arXiv:1911.07173 (2019).

279 [38] F.P. Bundy, K.J. Dunn, Phys. Rev. Lett. 44, 1623 (1980).

280 [39] Q. Liu, F. Fei, B. Chen, X. Bo, B. Wei, S. Zhang, M. Zhang, F. Xie, M. Naveed,
281 X. Wan, F. Song, B. Wang, Phys. Rev. B 99, 155119 (2019).

282 [40] H. Chi, C. Zhang, G. Gu, D.E. Kharzeev, X. Dai, Q. Li, New J. Phys. 19, 015005
283 (2017).

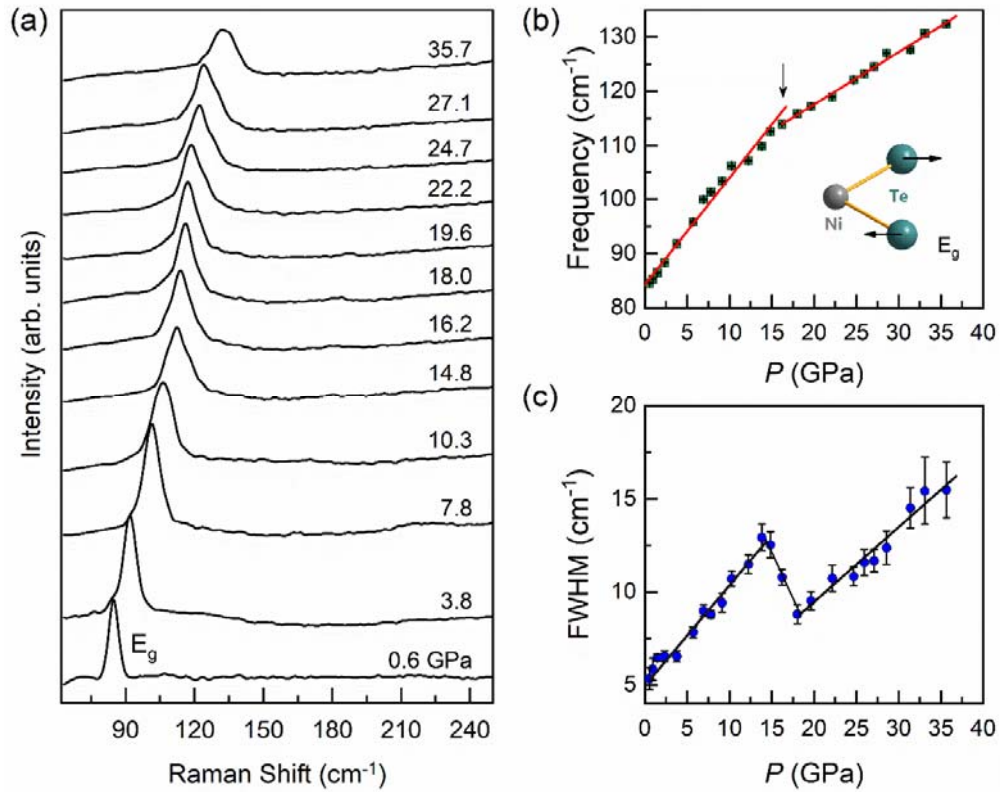
284
285



288

289 **FIG. 1.** High-pressure powder synchrotron XRD patterns of NiTe₂ at room
 290 temperature ($\lambda = 0.4133 \text{ \AA}$). (a) Representative diffraction patterns under compression
 291 up to 52.2 GPa. Le Bail refinement with $P\text{-}3m1$ space group is shown for 0.5 GPa.
 292 The open circles and red line represent the observed and calculated data, respectively.
 293 The vertical bars indicate the position of Bragg peaks. (b) The pressure-dependent
 294 lattice parameter a , c , and axis ratio c/a . (c) Volume as a function of pressure. The
 295 open circles denote the data of hexagonal ($P\text{-}3m1$, $Z = 1$) phase. The solid line is the
 296 fitting result based on the third-order Birch-Murnaghan equation of state.

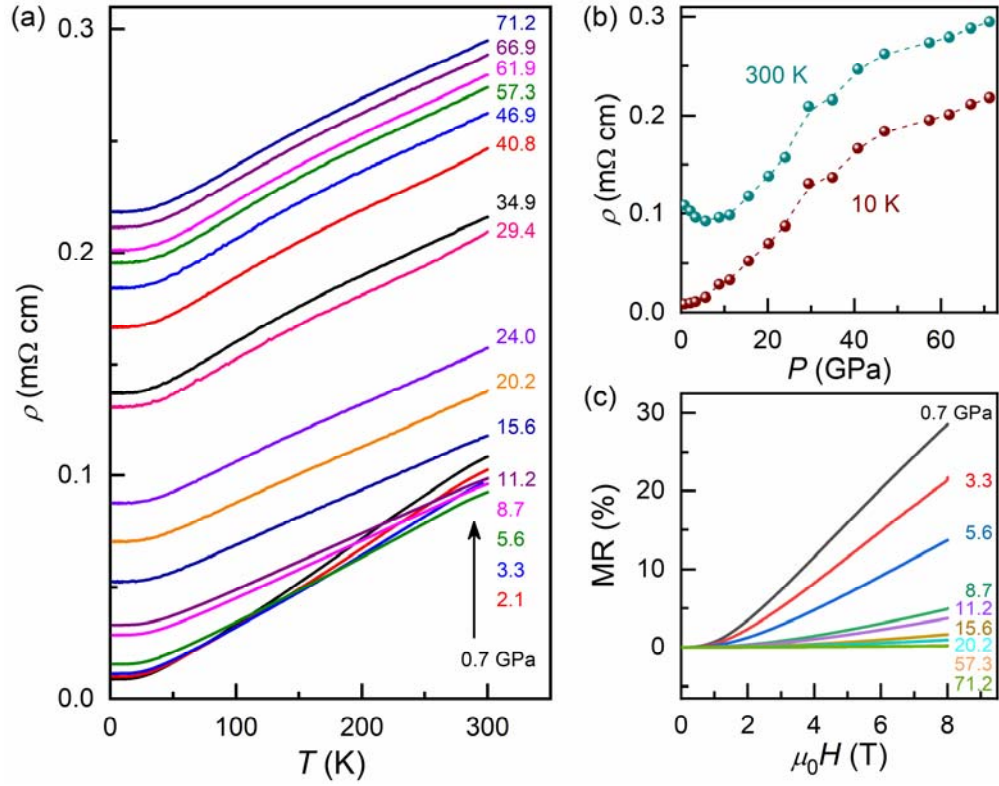
297



298

299 **FIG. 2.** (a) Pressure-dependent Raman spectra of NiTe₂ single crystal at room
 300 temperature. (b) The frequency of E_g mode as a function of pressure. The red solid
 301 lines represent linear fittings. Inset: The schematic view of Raman mode E_g. (c)
 302 Pressure dependence of FWHM of E_g mode. The black solid lines are guides to the
 303 eyes.

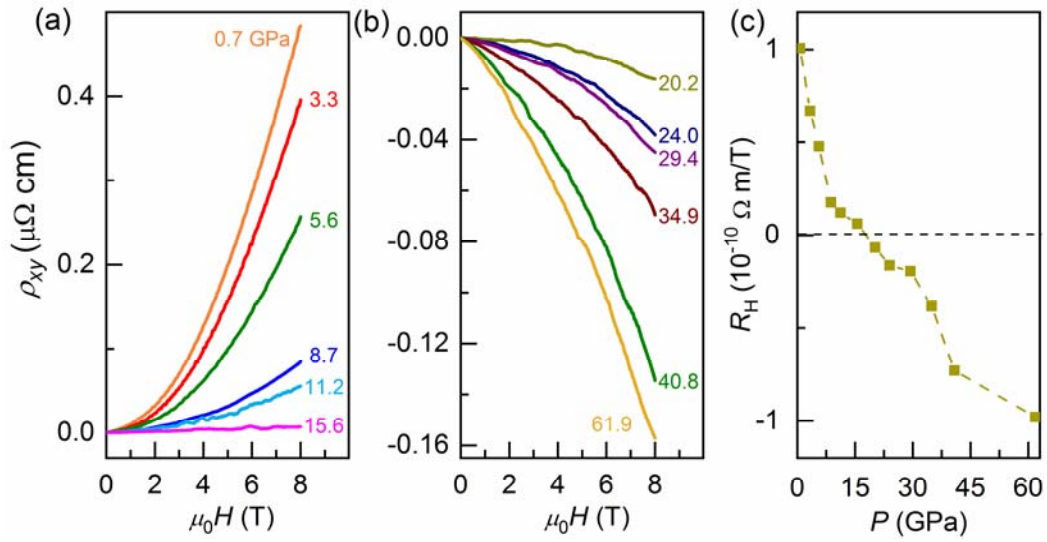
304



305

306 **FIG. 3.** (a) In-plane longitudinal resistivity curves $\rho(T)$ of NiTe₂ single crystal at
 307 various pressures up to 71.2 GPa. (b) Resistivity at 10 K and 300 K as a function of
 308 pressure. (c) Representative magnetoresistance curves of NiTe₂ single crystal at 10 K
 309 under pressure.

310



311

312 **FIG. 4.** (a,b) Pressure dependence of transversal Hall resistivity curves $\rho_{xy}(H)$ of
 313 NiTe_2 single crystal at 10 K. (c) Hall coefficient R_H as a function of pressure. The R_H
 314 is determined from the initial slope of $\rho_{xy}(H)$ at $H \rightarrow 0$.

315